High resolution spectral-domain optical coherence tomography at 1.3 micron center wavelength using a broadband superluminescent diode light source

Masreshaw Bayleyegn, Houssine Makhlouf, Caroline Crotti, Karsten Plamann, Arnaud Dubois

Ultrahigh Resolution Spectral-Domain Optical Coherence Tomography at 1.3 µm Using a Broadband Superluminescent Diode Light Source

Masreshaw D. Bayleyegn[1]*, Houssine Makhlouf[1], Caroline Crotti[2], Karsten Plamann[2], Arnaud Dubois[1]

[1]Laboratoire Charles Fabry, Institut d'Optique Graduate School, CNRS UMR 8501, Université Paris-Sud, 2 avenue Augustin Fresnel, 91127 Palaiseau cedex, France
[2] Laboratoire d'Optique Appliquée, ENSTA ParisTech – École Polytechnique – CNRS UMR 7639, Chemin de la Hunière, 91761 Palaiseau cedex, France
** Corresponding author: masreshaw.bayleyegn@institutoptique.fr Tel: +33 (0)1 64 53 34 36*

Abstract: We present an ultrahigh resolution spectral-domain optical coherence tomography imaging system using a broadband superluminescent diode light source emitting at a center wavelength of 1.3 µm. The light source consists of two spectrally shifted superluminescent diodes that are coupled together into a single mode fiber. The effective emission power spectrum has a full width at half maximum of 200 nm and the source output power is 10 mW. The imaging system has an axial resolution of 3.9 µm in air (< 3.0 µm in biological tissue), and a lateral resolution of 6.5 µm. The sensitivity and the maximum line rate are 95 dB and 46 kHz, respectively. Images of an infrared viewing card and a cornea from human eye suffering from glaucoma showing Schlemm's canal are presented to illustrate the performance of the system.

Keywords: Biomedical imaging, Optical coherence tomography, Superluminescent diode

1. Introduction

Optical Coherence Tomography (OCT) is a modern optical imaging technology that can perform cross-sectional imaging of biological tissues and semi-transparent materials in real-time at micrometer-scale resolution [1, 2]. OCT has been employed for *in situ* and *in vivo* biomedical imaging [3] as well as material characterization [4]. The most significant impact of OCT occurs in ophthalmology for retinal imaging [5, 6] and measurement of the dimensions of the anterior segment of the eye [7, 8].

To resolve fine sample structures at micrometer-scale, there has been a growing interest towards improving the spatial resolution achieved by OCT systems. Since OCT is based on low-coherence interferometry, the axial image resolution depends on the center emission wavelength and spectral bandwidth of the light source. High resolution OCT imaging requires the use of broadband light sources. Ultrahigh resolution time-domain OCT (TD-OCT) systems were demonstrated using femtosecond solid-state lasers [9] and continuum generation-based light sources [10]. However, such light sources are bulky, expensive and sensitive to misalignment. In comparison, superluminescent diode (SLD) sources are compact, robust, easy to operate and cost-effective. Since the emission spectrum of a single SLD is not broad enough for ultrahigh resolution OCT imaging, wavelength-division multiplexing of several spectrally shifted SLDs can be done to broaden the spectrum and provide higher axial resolution than currently possible with one SLD alone. A TD-OCT system with a measured axial resolution of 3.2 μm in the retina was demonstrated by multiplexing two SLDs to achieve an emission power spectrum with a full width at half maximum (FWHM) of 155 nm centered at a wavelength of 890 nm [11]. However, dual-band experiments in scattering biological samples demonstrated the superiority of OCT systems operating at 1.3 μm center wavelength compared to those operating at 0.8 μm in terms of imaging depth [12, 13]. But since the axial resolution is proportional to the square of the center emission wavelength and inversely proportional to the spectral bandwidth (see Eq. (1)), the spectral bandwidth of emission at 1.3 μm center wavelength needs to be 2.6 times larger than the one at 0.8 μm to maintain the axial resolution. Hence, getting a broadband light source and dealing with the subsequent dispersion issues are the challenges of ultrahigh resolution OCT at 1.3 μm center wavelength.

In addition to ultrahigh resolution, biomedical imaging applications require high speed and high detection sensitivity to perform real-time imaging with large penetration depth. As a consequence, Fourier-Domain OCT (FD-OCT) techniques are increasingly employed compared to TD-OCT because they offer significantly better sensitivity [14] and imaging speed [15]. In FD-OCT techniques, the depth information is retrieved by Fourier transforming the power spectrum of the interferometric signal. Depending on the technical approach used for acquiring the OCT spectral interferogram, two types of FD-OCT techniques can be distinguished: swept-source OCT (SS-OCT) and spectral-domain OCT (SD-OCT). In SS-OCT, a tunable light source and a single-element detector are employed. The emission wavelength of the light source is rapidly swept and the interferometric signal is recorded as a function of time [16]. In SD-OCT, a broadband light source and a spectrometer are used. The interferometric signal is obtained from the spectrometer directly as a function of spectral coordinate [17].

In this report, we present an ultrahigh resolution SD-OCT system operating at a center wavelength of 1.3 μm. The system uses a broadband light source consisting of two spectrally shifted SLDs that are coupled together into a single mode fiber. The SD-OCT system is characterized in terms of performance and compared to a commercial SS-OCT system operating

at the same center wavelength of 1.3 μm. Images of an infrared viewing card and a cornea from human eye suffering from glaucoma showing the Schlemm's canal are presented.

2. Principles and methods

2.1. Principles

The principle of SD-OCT relies on low-coherence light interferometry and detection of spectral interferograms by a spectrometer [17]. A beam emitted by a broadband light source is split into the sample arm and the reference arm of an interferometer. Light backscattered from different depths in a sample, which correspond to various optical delays, interferes with light reflected back from a reference mirror located at a fixed position. At the output of the interferometer, the interfering light is acquired by a grating-based spectrometer. Spectral components are detected by a linear array of photo-detectors. For a given optical path difference between the backscattering feature and the reference mirror, destructive and constructive interference occurs depending on the spectral component. This results in a modulated power spectrum at the output of the spectrometer. The modulation frequency is related to the optical path difference associated with the depth location of the backscattering feature within the sample. The modulation depth is proportional to the intensity of the backscattered light. The intensity-based depth profile of the sample is then reconstructed by calculating the Fourier transform of the acquired spectral interferogram after appropriate data re-sampling as explained in section 2.2. The main advantage of SD-OCT compared to TD-OCT is that the entire depth information is obtained from a single spectral interferogram in one shot without any mechanical scanning. This explains why SD-OCT is inherently faster than TD-OCT because in TD-OCT the depth reflectivity profile in the sample is sequentially acquired in time by mechanically scanning the optical path length in the reference arm.

The raw OCT data can be expressed as the sum of a strong DC term, an autocorrelation term and a cross-correlation term [18]. As the DC term is independent of optical path length difference, it contains no useful information about the sample structure and it can easily be removed by recording a background signal at the beginning of the experiment, by blocking the sample arm and reference arm separately, and subtracting it from the interferometric signal. In the case of strongly backscattering samples, the autocorrelation term associated with the mutual interference between all elementary waves scattered within the sample may significantly obscure the true sample structure that is given by the cross-correlation term. For such samples, sophisticated phase-shifting methods can be used to remove the autocorrelation term [18, 19]. However, such techniques increase the complexity of the system and data acquisition time. In practice, the autocorrelation term shows as structures at shallow depths in OCT images. It is customary to displace the reference mirror so that the surface of the sample shows at a location beyond the autocorrelation structures, and then the shallow depth range is numerically zeroed in the image.

2.2. Methods

The experimental setup of our ultrahigh resolution SD-OCT system, based on a free-space Michelson interferometer, is shown in Fig. 1. The illuminating light source consists of a combination of two spectrally shifted broadband SLDs. The emission spectrum of each SLD was measured by the OCT spectrometer and is shown in Fig. 2 (dotted curves). SLD 1 emits light at a center wavelength of 1233 nm with a spectral bandwidth (FWHM) of 80 nm, while SLD 2 emits light at a center wavelength of 1335 nm with a spectral bandwidth of 110 nm. The combination

of the two SLDs results in a broadband light source that has a spectral bandwidth of 200 nm (Fig. 2, solid curve). The combined broadband SLD light source provides shorter coherence length and better axial resolution than we could get with one SLD alone. The emission spectrum of the combined SLD light source is centered at 1300 nm wavelength, and the maximum output power is 10 mW. The spectral bandwidth, the emission spectrum shape and the output power of the combined SLD light source can be controlled to a certain extent by independently changing the current drive and the temperature control of each SLD. Light from the source is split between the sample arm and the reference arm by a 50/50 cube beam splitter. A telecentric scan lens (Thorlabs, LSM02) focuses light onto the sample and collects the backscattered light. A galvanometer-mounted mirror in the sample arm enables transverse beam scanning on the sample. In the reference arm, light is back-reflected by a silver mirror and interferes with the backscattered light from the sample at the output of the interferometer. A dispersion compensator (Thorlabs, LSM02DC) in the reference arm introduces a similar magnitude of dispersion as that of the scan lens placed in the sample arm to correct for the dispersion mismatch between the two arms. A variable attenuator is placed in front of the reference mirror to attenuate light returning from the reference arm. The attenuator is adjusted to optimize the modulation depth of the raw OCT interference term, hence the OCT signal sensitivity [20]. A spectrometer, located at the output of the interferometer, consists of a diffraction grating (600 lines/mm), an achromatic doublet (120 mm focal length) and an InGaAs linear array detector (Goodrich, SU-LDH Digital Line Scan Camera, 1024 pixels). The linear array camera acquires the spectral interferogram and transfers the 14-bit digital data to a personal computer equipped with an image acquisition card (National Instruments, NI PCIe-1427). The maximum line rate of the camera is 46 kHz.

The axial profile of the sample (A-scan) is reconstructed from the acquired spectral interferogram by fast Fourier transform (FFT) after data re-sampling. In FD-OCT, the structural information of the sample is encoded in the modulation frequencies of wavenumber (k) dependent spectral fringes. However, a grating-based spectrometer in SD-OCT gives a spectral interferogram that is almost evenly sampled with respect to wavelength (λ), and as λ and k are inversely related, the dataset will be non-evenly sampled with respect to k. In order to apply the FFT and reconstruct the depth profile, the dataset needs to be first evenly sampled in k space. A spectral calibration method based on phase linearization was employed to achieve this relevant re-sampling [21]. In this method, an attenuated single reflector is placed in the sample arm at a given location beyond the optical path match condition. Had the spectrum been evenly sampled in k space, this single reflector would yield a raw SD-OCT signal having a single modulation frequency. However, the acquired spectral interferogram that is plotted in Fig. 3(a) (intensity scale on the left axis) as a function of CCD pixel number shows a distorted modulation pattern. The FFT of this spectral interferogram gives a broadened axial point-spread function (PSF) as shown in Fig. 3(b) (dotted curve). The phase associated with the distorted modulation pattern is extracted by a computer algorithm. It is plotted in Fig. 3(a) (phase scale on the right axis) and shows a non-linear trend. The phase is then linearized and the corresponding camera pixel indices are interpolated at those evenly spaced values of the phase. Finally, the spectral interferogram is interpolated at the new pixel indices. The corresponding axial PSF obtained after re-sampling (correction) is shown in Fig. 3(b) (solid curve). All the subsequently acquired raw SD-OCT data are interpolated at the new pixel index values determined by the above spectral calibration to obtain properly sampled data in k space.

The image processing algorithm and user friendly control and display software were developed using LabView. During lateral scanning of the illumination beam on the sample,

multiple A-scans are acquired and processed. At the end of the scanning cycle, an intensity-based cross-sectional image (B-scan) of the sample is reconstructed and displayed on the computer screen.

3. System performance

3.1. Spatial resolutions

The transverse resolution of images obtained from OCT systems, like other scanning imaging systems, is determined by the size of the focused beam spot on the sample which depends on the focusing optics and the wavelength of the illuminating light. With a collimated Gaussian beam profile having a beam diameter of 4.6 mm and a scan lens with an effective focal length of 18 mm, the transverse resolution of our SD-OCT is 6.5 µm.

The axial resolution of OCT is determined by the spectral bandwidth $\Delta\lambda$ and center wavelength λ_o of the light source that illuminates that illuminates the sample. For a light source with a Gaussian-shaped emission spectrum and with no dispersion mismatch between the two arms of the interferometer, the axial resolution Δz is given by [22]

$$\Delta z = \frac{2\ln 2}{\pi n} \times \frac{\lambda_o^{\,2}}{\Delta\lambda}\ , \tag{1}$$

where n is the refractive index of the sample. Equation (1) indicates that a broader spectral bandwidth leads to a higher axial resolution. In our system, the combination of the two SLDs with different center emission wavelengths provides a larger spectral bandwidth and therefore a higher axial resolution than what can be achieved using one SLD alone. The reported SD-OCT system achieves a theoretical axial resolution of 3.7 µm in air, which corresponds to 2.7 µm in biological tissue with a refractive index of $n \sim 1.4$. Experimentally, the axial resolution in SD-OCT suffers not only from the constant dispersion mismatch between the two arms, which we have minimized by using a dispersion compensator, but also from the uneven sampling of the spectral interferogram, which we have corrected as explained in section 2.2. The experimental axial resolution of our system was determined by measuring the FWHM of the PSF obtained after correction as shown in Fig. 3(b) (solid curve). At an arbitrary depth of 310 µm, the axial resolution was measured to be 3.9 µm in air (2.8 µm in tissue).

3.2. Dynamic range and sensitivity

Dynamic range (DR) refers to the ratio between the highest and the lowest measurable signals [6]. A camera with high DR is required in SD-OCT to be able to capture the modulating part of the raw OCT signal that is weak relative to the strong DC part. For shot-noise limited detection, the DR is proportional to the full-well capacity of the camera [6]. A DR of 70 dB can be reached with our InGaAs line camera, depending on the gain capacitor setting. The 14-bit digitization of the camera guarantees that the analog-to-digital convertor faithfully renders all the levels of the captured analog signal into a useable digital output for further digital processing. A higher gain capacitor improves the dynamic range at the cost of increasing the readout noise.

Detection sensitivity Σ of OCT systems is a measure of the smallest sample reflectivity $R_{s,\min}$ that can be detected. It is determined by the signal level at which the signal-to-noise ratio (SNR) equals one. Σ is expressed as a function of $R_{s,min}$ by [23]

$$\sum[dB] = 10 \times \log\left(\frac{1}{R_{s,\min}}\right). \tag{2}$$

We have experimentally characterized the sensitivity of our SD-OCT system by using a silver mirror as a sample and placing a neutral density (ND) filter with a density value D = 2 in front of the mirror. Considering a double pass through the ND filter, the combination of the mirror and the ND filter corresponds to an equivalent sample reflectivity of 10^{-4}. A typical PSF obtained in this configuration after performing the required spectral re-sampling (see section 2.2) and FFT is shown in Fig. 4. The vertical axis in Fig. 4 gives the reflectivity expressed in decibels (- 40 dB corresponds to a reflectivity of 10^{-4}). The noise level corresponds to the minimal sample reflectivity that can be detected by our SD-OCT system, defined as the sensitivity $\sum$. It was measured to be Σ = 95 dB. Inverting equation (2) enables one to calculate the corresponding minimal detectable reflectivity $R_{s,min} = 3.16\times10^{-10}$. A variable attenuator in the reference arm helps to match the experimental conditions during system characterization and imaging of actual samples.

3.3. Imaging depth and sensitivity fall-off

The maximal imaging depth z_{max} of SD-OCT is determined by the spectral sampling resolution $\delta\lambda$ of the spectrometer and is expressed by [24]

$$z_{\max} = \frac{1}{4n} \times \frac{\lambda_o^{\,2}}{\delta\lambda}. \tag{3}$$

In the reported SD-OCT system, a total spectral bandwidth of 245 nm was dispersed across the 1024 pixels of the linear detector (see Fig. 2), resulting in a spectral sampling $\delta\lambda$ of 0.24 nm. The theoretical imaging depth $z_{\max}$ was calculated to be 1.8 mm in air (~ 1.3 mm in tissue), and is in agreement with the imaging depth observed experimentally by translating a single reflector axially in the sample arm. Experimental studies of tissue absorption and scattering have shown that the number of ballistic photons used to image biological tissues using OCT decreases exponentially as a function of depth [25]. The useful imaging depth of SD-OCT in a biological specimen is in fact limited not only by the attenuation of ballistic light but also by the depth dependent sensitivity fall-off of the imaging system.

In SD-OCT, the depth dependent sensitivity fall-off, even without absorption or scattering from the sample, is due to washout of spectral fringe visibility primarily caused by the limited spectral sampling resolution of the spectrometer to resolve high frequency spectral fringes that correspond to large depths [24, 26]. Another factor that contributes to the depth dependent signal fall-off which becomes even worse for high resolution SD-OCT is partial aliasing [27] due to the non-uniform sampling of the spectrum in wavenumber. To characterize the sensitivity fall-off of the reported SD-OCT system as a function of imaging depth, we repeated the sensitivity characterization experiment (see section 3.2) for different axial positions of the mirror used as a sample, while keeping the reflected sample arm power unchanged. Compared to the signal peak value in the proximity of zero path length difference, the sensitivity fall-off at a depth of 1 mm was found to be less than 6 dB. At the maximal imaging depth of our system (1.76 mm), the sensitivity fall-off was measured to be ~ 13 dB. Various hardware modifications [27-29] and advanced image reconstruction methods [26] have been reported to reduce the sensitivity fall-off, but at the cost of more hardware complexities and/or increased image acquisition and processing time.

4. Image results

The reported SD-OCT system was compared in terms of image quality with a commercial SS-OCT system (Thorlabs, OCS1300SS) operating at the same center wavelength of emission and providing images with a spatial resolution of 12 µm×25 µm (axial×transverse). An infrared viewing card (Thorlabs, model VRC5) was used as a test sample. The cross-sectional OCT images shown in Fig. 5(a) and 5(b) were obtained using the SD-OCT system and the commercial SS-OCT system, respectively. The images reveal the internal structures of the card. Three distinct layers can be distinguished. The upper layer corresponds to a plastic material with a thickness of 170 µm. A random distribution of scattering structures is revealed inside this polymer material. The bottom layer is very inhomogeneous and corresponds to the photosensitive material. The middle layer, in contrast, is very homogeneous since no scattered light is detected from this region. This layer is assumed to be the glue used for bonding the photosensitive material to the plastic layer. These OCT images demonstrate the improvement of resolution when using the SD-OCT system.

As part of a collaborative project on glaucoma surgery, we also imaged samples of excised human corneas. Glaucoma is an eye disorder that usually develops as a result of increased intraocular pressure (IOP) of the eye due to the accumulation of a fluid called aqueous humor. It can permanently damage vision and lead to blindness if not treated. In a healthy eye, most of the outflow of the aqueous humor occurs through a circular channel called Schlemm's canal [30]. In glaucomatous eye, it is believed that the principal site of the fluid outflow resistance is related to the Schlemm's canal [31]. For the research project, human corneas not suitable for transplantation because of low endothelial cell density or small optical zone (< 8 mm) were obtained from the *Banque Française des Yeux* (French Eye Bank, Paris, France). The study was conducted according to the tenets of the Declaration of Helsinki and the French legislation for scientific use of human corneas.

Unlike the transparent fibers in healthy cornea, the sclera (white part of the eye) is made up of opaque fibers that strongly scatter light. Moreover, glaucomatous cornea, cornea from a person with glaucoma, scatters more light than a healthy cornea. This is partly because of the fact that glaucoma and corneal edema often co-exist [32]. It has been observed that there is a high incidence of endothelial dystrophies among patients with glaucoma [33]; and one of the clinical manifestations of endothelial dystrophies is corneal edema [34]. Moreover, the persistent elevated IOP, which is often the case of glaucoma, creates high pressure gradient against stroma that drives the aqueous humor from the anterior chamber across endothelium into stroma, affecting corneal hydration and hence corneal edema [35, 36]. A cross-sectional image of excised cornea with a sclera rim of a human eye suffering from glaucoma is shown in Fig. 6. The two arrows in the OCT image indicate the Schlemm's canal that is located at a depth of ~ 0.8 mm inside the corneoscleral junction of human eye suffering from glaucoma. This demonstrates that the choice of the wavelength region around 1.3 µm helps to maximize the imaging depth in a highly scattering biological tissue.

5. Conclusions

We have presented an ultrahigh resolution SD-OCT imaging system operating at a center emission wavelength of 1.3 µm using a compact broadband light source consisting of two multiplexed SLDs with shifted spectral properties. The spectral region around this center wavelength is optimal for its reduced absorption and low tissue scattering. As a result, imaging depth in biological samples is maximized. The SD-OCT imaging system has an axial resolution

of 3.9 µm in air, which corresponds to 2.8 µm in typical biological tissues, and a lateral resolution of 6.5 µm. The sensitivity and the maximum line rate of the system are 95 dB and 46 kHz, respectively. For ultrahigh resolution OCT, using compact, robust and cost-effective SLD light sources is more convenient than using bulky and expensive femtosecond lasers or supercontinuum-generation based sources. Images of different samples were shown to illustrate the performance of the system. In particular, we have demonstrated the possibility of imaging the Schlemm's canal located at a relatively large depth inside a highly scattering corneoscleral junction of a human eye suffering from glaucoma. This paves the way to using ultrahigh resolution SD-OCT imaging systems at 1.3 µm for guiding glaucoma laser surgery. Currently, we are doing research on the development of a new tool for glaucoma surgery. A femtosecond laser will be used to cut in the resistive region around the Schlemm's canal, which will facilitate the drainage of the fluid. The ultrahigh resolution SD-OCT reported here will be employed to guide the laser cutting.

Acknowledgments

This work was supported by the Agence Nationale de la Recherche under the project NOUGAT, ANR-08-TECS-012, program TecSan.

Reference

[1] D. Huang, E.A. Swanson, C.P. Lin, J.S. Schuman, W.G. Stinson, W. Chang, M.R. Hee, T. Flotte, K. Gregory, C.A. Puliafito, J.G. Fujimoto, Optical Coherence Tomography, Science, 254 (1991) 1178-1181

[2] A.F. Fercher, Optical coherence tomography, J. Biomed. Opt., 1 (1996) 157-173.

[3] J.G. Fujimoto, Optical coherence tomography for ultrahigh resolution in vivo imaging, Nat. Biotechnol., 21 (2003) 1361 - 1367

[4] K. Wiesauer, M. Pircher, E. Götzinger, S. Bauer, R. Engelke, G. Ahrens, G. Grützner, C.Hitzenberger, D.Stifter, En-face scanning optical coherence tomography with ultra-high resolution for material investigation, Opt. Express 13 (2005) 1015-1024.

[5] E.A. Swanson, J.A. Izatt, M.R. Hee, D. Huang, C.P. Lin, J.S. Schuman, C.A. Puliafito, J.G. Fujimoto, In vivo retinal imaging by optical coherence tomography, Opt. Lett., 18 (1993) 1864-1866.

[6] M. Wojtkowski, R. Leitgeb, A. Kowalczyk, T. Bajraszewski, A.F. Fercher, In-vivo human retinal imaging by Fourier domain optical coherence tomography, J. Biomed. Opt. , 7 (2002) 457-463.

[7] J.A. Izatt, M.R. Hee, E.A. Swanson, C.P. Lin, D. Huang, J.S. Schuman, C.A. Puliafito, J.G. Fujimoto, Micrometer-scale resolution imaging of the anterior eye in vivo with optical coherence tomography, Arch. Ophthalmol. , 112 (1994) 1584-1589.

[8] S. Trefford, F. Desmond, Optical Coherence Tomography of the Anterior Segment, Ocul. Surf. , 6 (2008) 117-127

[9] W. Drexler, U. Morgner, F.X. Kärtner, C. Pitris, S.A. Boppart, X.D. Li, E.P. Ippen, J.G. Fujimoto, In vivo ultrahigh-resolution optical coherence tomography, Opt. Lett., 24 (1999) 1221-1223.

[10] I. Hartl, X.D. Li, C. Chudoba, R.K. Ghanta, T.H. Ko, J.G. Fujimoto, J.K. Ranka, R.S. Windeler, Ultrahigh-resolution optical coherence tomography using continuum generation in an air-silica microstructure optical fiber, Opt. Lett., 26 (2001) 608-610.

[11] T. Ko, D. Adler, J. Fujimoto, D. Mamedov, V. Prokhorov, V. Shidlovski, S. Yakubovich, Ultrahigh resolution optical coherence tomography imaging with a broadband superluminescent diode light source, Opt. Express, 12 (2004) 2112-2119.

[12] Y. Pan, D. Farkas, Noninvasive imaging of living human skin with dual-wavelength optical coherence tomography in two and three dimensions, J. Biomed. Opt.Vol.3, pp. 446-455., 3 (1998) 446-455.

[13] D. Sacchet, J. Moreau, P. Georges, A. Dubois, Simultaneous dual-band ultra-high resolution full-field optical coherence tomography, Opt. Express, 16 (2008) 19434-19446.

[14] M. Choma, M. Sarunic, C. Yang, J. Izatt, Sensitivity advantage of swept source and Fourier domain optical coherence tomography, Opt. Express, 11 (2003) 2183-2189.

[15] S. Yun, G. Tearney, B. Bouma, B. Park, J. de Boer, High-speed spectral-domain optical coherence tomography at 1.3 μm wavelength, Opt. Express, 11 (2003) 3598-3604.

[16] S.R. Chinn, E.A. Swanson, J.G. Fujimoto, Optical coherence tomography using a frequency-tunable optical source, Opt. Lett., 22 (1997) 340-342.

[17] A.F. Fercher, C.K. Hitzenberger, G. Kamp, S.Y. El-Zaiat, Measurements of intraocular distances by backscattering spectral interferometry, Opt. Comm., 117 (1995).

[18] M. Wojtkowski, A. Kowalczyk, R. Leitgeb, A.F. Fercher, Full range complex spectral optical coherence tomography technique in eye imaging, Opt. Lett., 27 (2002) 1415-1417.

[19] R.A. Leitgeb, C.K. Hitzenberger, A.F. Fercher, T. Bajraszewski, Phase-shifting algorithm to achieve high-speed long-depth-range probing by frequency-domain optical coherence tomography, Opt. Lett., 28 (2003) 2201-2203.

[20] R. Leitgeb, W. Drexler, A. Unterhuber, B. Hermann, T. Bajraszewski, T. Le, A. Stingl, A. Fercher, Ultrahigh resolution Fourier domain optical coherence tomography, Opt. Express, 12 (2004) 2156-2165.

[21] H. Makhlouf, Integrated multimodal-spectral fluorescence confocal microscope and spectral-domain optical coherence tomography imaging system for tissue screening, Faculty of College of Optical Sciences, The University of Arizona, 2011, pp. 181.

[22] E.A. Swanson, D. Huang, M.R. Hee, J.G. Fujimoto, C.P. Lin, C.A. Puliafito, High-speed optical coherence domain reflectometry, Opt. Lett., 17 (1992) 151-153.

[23] R. Leitgeb, C. Hitzenberger, A. Fercher, Performance of fourier domain vs. time domain optical coherence tomography, Opt. Express, 11 (2003) 889-894.

[24] G. Häusler, M.W. Lindner, "Coherence Radar" and "Spectral Radar"—New Tools for Dermatological Diagnosis, J. Biomed. Opt., 3 (1998) 21-31.

[25] G. Popescu, A. Dogariu, Ballistic Attenuation of Low-Coherence Optical Fields, Appl. Opt., 39 (2000) 4469-4472.

[26] K. Wang, Z. Ding, T. Wu, C. Wang, J. Meng, M. Chen, L. Xu, Development of a non-uniform discrete Fourier transform based high speed spectral domain optical coherence tomography system, Opt. Express, 17 (2009) 12121-12131.

[27] T. Bajraszewski, M. Wojtkowski, M. Szkulmowski, A. Szkulmowska, R. Huber, A. Kowalczyk, Improved spectral optical coherence tomography using optical frequency comb, Opt. Express, 16 (2008) 4163-4176.

[28] Z. Wang, Z. Yuan, H. Wang, Y. Pan, Increasing the imaging depth of spectral-domain OCT by using interpixel shift technique, Opt. Express, 14 (2006) 7014-7023.

[29] Z. Hu, A.M. Rollins, Fourier domain optical coherence tomography with a linear-in-wavenumber spectrometer, Opt. Lett., 32 (2007) 3525-3527.

[30] R. Avtar, R. Srivastava, Aqueous outflow in Schlemm's canal, Applied Mathematics and Computation, 174 (2006) 316-328.

[31] M.C. Johnson, R.D. Kamm, The role of Schlemm's canal in aqueous outflow from the human eye, Invest Ophthalmol Vis Sci., 24(3) (1983) 320-325.

[32] R.S. Figueiredo, S.V. Araujo, E.J. Cohen, C.J. Rapuano, L.J. Katz, R.P. Wilson, Management of coexisting corneal disease and glaucoma by combined penetrating keratoplasty and trabeculectomy with mitomycin-C, Ophthalmic Surgery and Lasers 27 (1996) 903-909.

[33] F. Bigar, R. Witmer, Corneal endothelial changes in primary acute angle-closure glaucoma, Ophthalmology, 89 (1982) 596-599.

[34] G.O. Waring, M.M. Rodrigues, P.R. Laibson, Corneal dystrophies. II. Endothelial dystrophies, Surv Ophthalmol. , 23 (1978) 147-168.

[35] J. Ytteborg, C. Dohkman, Corneal Edema and Intraocular Pressure: Animal Experiments, Arch Ophthalmol., 74 (1965) 375-381.

[36] W.S. Vanmeter, W.B. Lee, D.G. Katz, Corneal Edema (Chapter 16A), Duane's Clinical Ophthalmology, Lippincott Williams and Wilkins 2006.

Figure captions

Fig. 1. Schematic diagram of the SD-OCT experimental setup.
GR, grating; FL, focusing lens; LSC, InGaAs line scan camera; SLD, superluminescent diode; CL, collimating lens; BS, beam splitter; GM, galvanometric-mounted mirror; DAQ, data acquisition board; PC, personal computer; DC, dispersion compensator; MO, microscope objective; ND, neutral density filter, RM, reference mirror.

Fig. 2. Emission power spectrum of the light source (solid curve) for SD-OCT
SLD 1 and SLD 2 (dotted curves representing the emission spectra) are combined to increase the spectral bandwidth of the illumination light source. The effective spectral bandwidth the light source is 200 nm at FWHM.

Fig. 3. Spectral interferogram and its axial PSF
a) The spectral interferogram (left axis) and the associated non-linear phase (right axis)
b) The corresponding axial PSF before correction (dotted curve) and after correction (solid curve) at 310 μm depth

Fig. 4. Sensitivity measurement of SD-OCT
A single A-scan of a mirror with neutral density filter of ND = 2 placed in the sample arm

Fig. 5. Comparison of two FD-OCT imaging systems
Cross-sectional image of an infra-red viewing card by SD-OCT (a) and SS-OCT (b). As can be seen, the ultrahigh resolution SD-OCT image provides detailed internal structures of the viewing card better than with the SS-OCT system working at the same center wavelength.

Fig. 6. Cross-sectional image of an excised corneosclera from glaucomatous eye showing the Schlemm's canal
The Schlemm's canal is an annular channel situated at nearly 0.8 mm depth from the external corneoscleral surface. It appears as two holes (indicated by arrows) in the cross-sectional image of the cornea. The hole on the right is wider than the hole on the left. This may be due to the collapse of one side of the channel while working *ex vivo*.

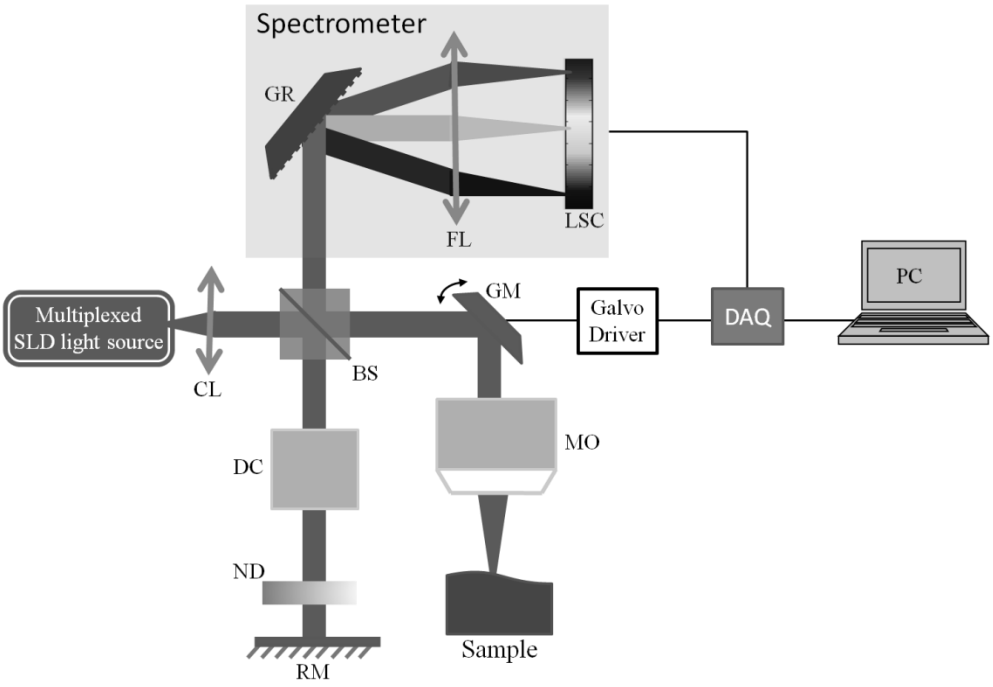

Fig. 1. Schematic diagram of the SD-OCT experimental setup
GR, grating; FL, focusing lens; LSC, InGaAs line scan camera; SLD, superluminescent diode; CL, collimating lens; BS, beam splitter; GM, galvanometric-mounted mirror; DAQ, data acquisition board; PC, personal computer; DC, dispersion compensator; MO, microscope objective; ND, neutral density filter, RM, reference mirror.

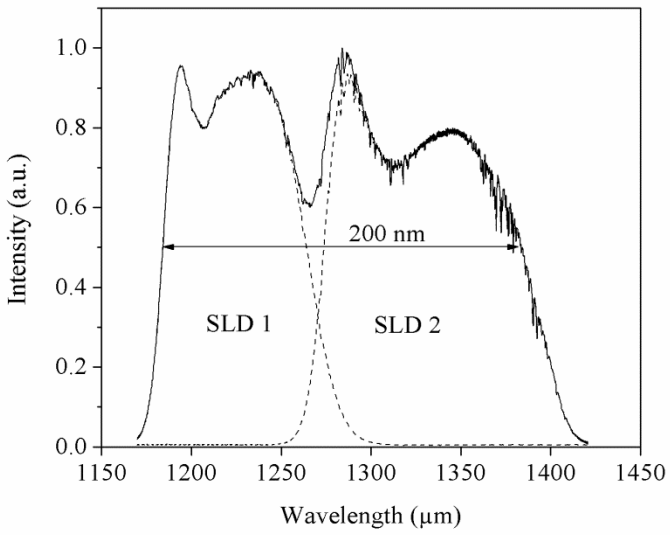

Fig. 2. Emission power spectrum of the light source (solid curve) for SD-OCT
SLD 1 and SLD 2 (dotted curves representing the emission spectra) are combined to increase the spectral bandwidth of the illumination light source. The effective spectral bandwidth the light source is 200 nm at FWHM.

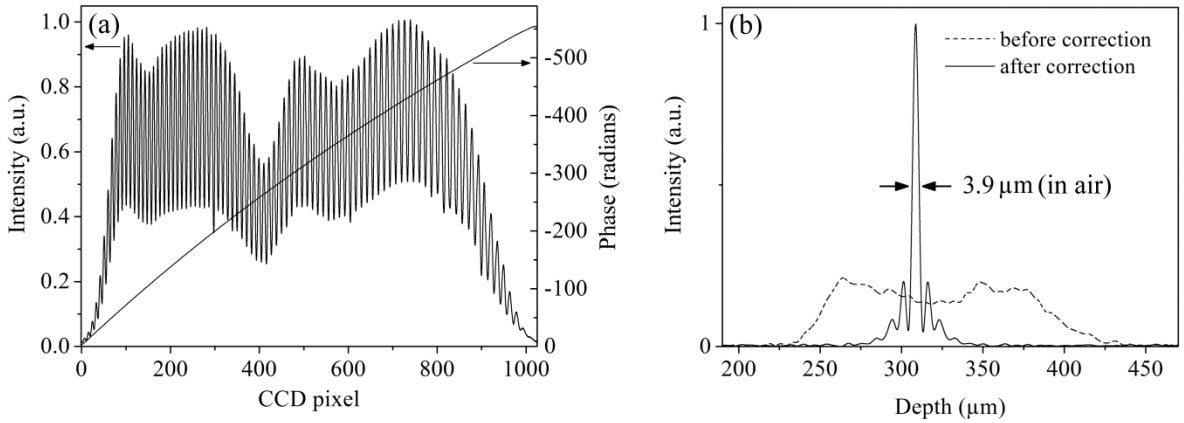

Fig. 3. Spectral interferogram and its axial PSF
a) The spectral interferogram (left axis) and the associated non-linear phase (right axis)
b) The corresponding axial PSF before correction (dotted curve) and after correction (solid curve) at 310 µm depth

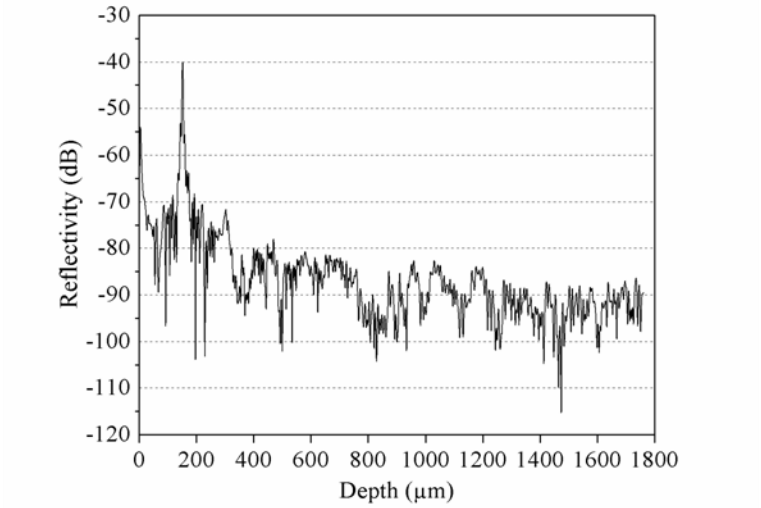

Fig. 4. Sensitivity measurement of SD-OCT
A single A-scan of a mirror with neutral density filter of ND = 2 placed in the sample arm

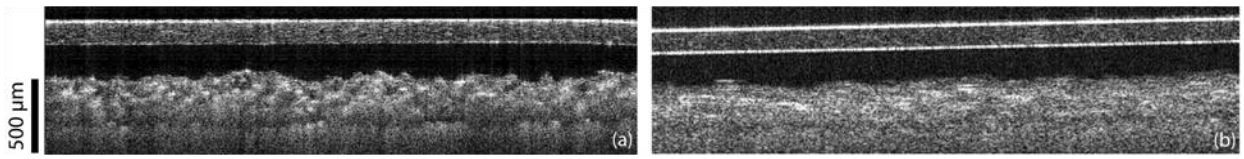

Fig. 5. Comparison of two FD-OCT imaging systems
Cross-sectional image of an infra-red viewing card by SD-OCT (a) and SS-OCT (b). As can be seen, the ultrahigh resolution SD-OCT image provides detailed internal structures of the viewing card better than with the SS-OCT system working at the same center wavelength.

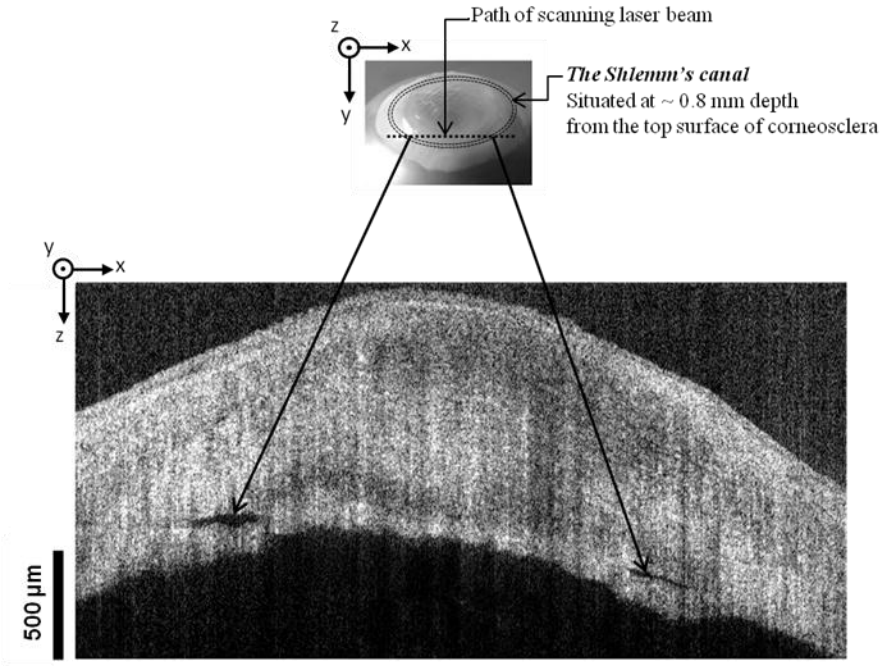

Fig. 6. Cross-sectional image of an excised corneosclera from glaucomatous eye showing the Schlemm's canal The Schlemm's canal is an annular channel situated at nearly 0.8 mm depth from the external corneoscleral surface. It appears as two holes (indicated by arrows) in the cross-sectional image of the cornea. The hole on the right is wider than the hole on the left. This may be due to the collapse of one side of the channel while working *ex vivo*.